PHYSICAL REVIEW A **70**, 013605 (2004)

# Manifestations of vortices during ultracold-atom propagation through waveguides

M. W. J. Bromley* and B. D. Esry†
*Department of Physics, Kansas State University, Manhattan, Kansas 66506, USA*
(Received 25 April 2004; published 12 July 2004)

The possibility of generating vortices during matter-wave propagation through microstructures is examined. Vortices can arise solely due to wave interference in low-density ultracold atom clouds, and do not require any atom–atom (nonlinear) interactions. The properties of these "interference vortices" are understood from a simple two-mode model in a straight waveguide. This model is then applied to vortex creation in a circular bend since a circular waveguide bend is one of the simplest atom optical elements that can induce mode excitations. Time-independent and time-dependent analyses are used to investigate vortex creation and dynamics in these systems.

DOI: 10.1103/PhysRevA.70.013605 PACS number(s): 03.75.Be, 03.75.Lm, 67.40.Vs, 42.25.Hz

## I. INTRODUCTION

Vortices in quantum mechanics have been known since its early days, tracing back to Dirac's seminal paper on wave-function holes and their vortices [1]. They have been predicted and observed in diverse fields of wave related physics (see Ref. [2] for an introduction), some examples of note are quantum chemistry reaction pathways [3], liquid helium as a consequence of superfluidity [4], ballistic electron transport through waveguides [5], and dilute atomic Bose-Einstein condensates (BECs) [6].

The recent advent of the atom chip, i.e., integrated atom optics above microchip surfaces [7], along with the recent demonstrations of BEC creation and propagation all on-chip [8] are creating further opportunities to perform precision wave-function engineering on the microscopic scale. Inspired by the vortex studies of ballistic electron transport through hard-walled waveguides [5,9,10], we examine the possibility of generating vortices during atomic matter-wave propagation through microstructures.

One mechanism for the formation of vortices is simple wave interference. Hirschfelder and collaborators, for example, examined vortex creation around wave-function holes for plane-wave scattering from 2-D potentials such as partially and totally reflecting walls [11,12]. In the present paper, the fundamental mechanism for generating what we call interference vortices (also known as optical vortices [13]) is examined using two simple geometries. We first explore the simplest conditions for vortices to occur in a straight waveguide by superposing plane waves that occupy different transverse modes. We then examine plane-wave and wave-packet propagation through a simple microstructure, the circular waveguide bend, essentially using the bend as a means to create multimoded low-density ultracold matter waves and thus vortices.

None of the vortices discussed here require atom–atom interactions, and will occur even for low densities. In fact, our investigations explicitly assume that atom–atom interactions are negligible. Vortices are familiar in systems with nonlinear interactions. Ruostekoski *et al.* [14], as a theoretical example, found vortices in an expanding BEC reflecting from the hard walls of a two-dimensional (2D) circular box. Indeed, there are a variety of ways that vortices can be produced in nonlinear optics (see Ref. [15] and references therein). The present interference vortices, however, do not demand the presence of a nonlinear interaction and do not have a critical velocity for vortex formation beyond the requirement of exciting transverse modes.

We chose to revisit [16,17] the circular bend geometry as it is a simple geometry that can easily be explored using both time-independent and wave-packet calculations. Furthermore, similar studies of ballistic electron transport have yielded intriguing vortex physics. In particular, the curved electron waveguide produces effects such as reversal of the flux direction around the wave-function holes as the energy crosses the resonance [10,18,19]. These effects were also extensively examined in plane-wave propagation through an L-shaped bend (intended to mimic chemical reaction pathways) [3].

These electron gas studies rarely consider wave packets. Given that BECs are the most likely source for atom optics, our interest was whether interference vortices could even be observed during wave-packet propagation, or whether they would simply be washed out by the continuum of velocities in a wave packet. We show that interference vortices are observed in wave packets and that their dynamics can be understood in terms of a simple two-mode model.

## II. VORTICES IN SUPERPOSITIONS OF PLANE WAVES

A simple system that exhibits interference vortices is a two-mode model of plane waves travelling down a straight waveguide. The model considered here constrains the two plane waves to have the same total energy, and thus the excited mode always has a lower velocity than the ground mode. This constraint is consistent with the physics of waves propagating through generic microstructures in that when a wave is excited by a static potential the total energy of the excited component remains conserved. The results of the simple model are later used to explain the dynamics of inter-

*Electronic address: bromley@phys.ksu.edu
†Electronic address: esry@phys.ksu.edu

 

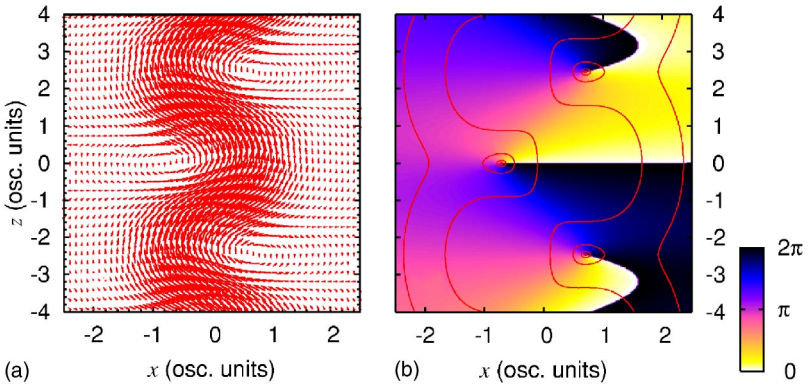


FIG. 1. (Color online) Superposition of equal amounts of two plane waves in the ground and first excited SHO transverse modes (in $x$). The waves propagate freely in the positive $z$ direction with the same total energy $E=1.51$. The local velocity $\vec{v}(x,z)$ is shown in (a) as a vector field, and (b) shows the local phase $\theta(x,z)$ along with contours of the probability density $|\psi(x,z)|^2$. Each contour corresponds to an order of magnitude change in density.

ference vortices in a multimoded wave packet.

To examine vortices in general, it is useful to turn to the hydrodynamical representation of the wave function [12],

$$\psi(\mathbf{r},t) = \sqrt{\rho(\mathbf{r},t)}e^{i\theta(\mathbf{r},t)/\hbar}, \tag{1}$$

where both the local density $\rho(\mathbf{r},t)=|\psi(\mathbf{r},t)|^2$ and the local phase $\theta(\mathbf{r},t)/\hbar=\arctan\{\mathrm{Im}[\psi(\mathbf{r},t)]/\mathrm{Re}[\psi(\mathbf{r},t)]\}$ are real quantities. The local velocity $\vec{v}(\mathbf{r},t)$ is related to the local flux $\vec{j}(\mathbf{r},t)$, and is given by

$$\vec{v}(\mathbf{r},t) = \frac{\vec{j}(\mathbf{r},t)}{\rho(\mathbf{r},t)} = \frac{\hbar}{m}\mathrm{Im}\left[\frac{\vec{\nabla}\psi(\mathbf{r},t)}{\psi(\mathbf{r},t)}\right]. \tag{2}$$

We use primarily the local phase throughout this paper since the probability density typically varies over orders of magnitude across the waveguide (and thus so does the local flux). Also, the local velocity can be large in regions of small probability density, making it difficult to plot a vector field that sufficiently highlights any spatial dependence.

Consider a superposition of two plane waves freely propagating in the $z$ direction, with transverse confinement in $x$ provided by a simple harmonic oscillator potential (SHO) centered at $x=0$:

$$\psi(x,z) = a_0\varphi_0(x)e^{iv_0z} + a_1\varphi_1(x)e^{iv_1z}, \tag{3}$$

where $\varphi_n(x)$ are the normalized SHO eigenfunctions and $a_n$ are the mixing coefficients. This wave function is an energy eigenstate, so the total energy $E$ available to each mode is a constant $v_n=\sqrt{2(E-E_n)}$. Oscillator units are used throughout this paper (i.e., $\hbar=1$, mass $m=1$, and the SHO frequency $\omega=1$). These units give an oscillator width $\beta=1$. To provide the typical scale of the SI units involved here, a cloud of $^{23}$Na atoms trapped with a frequency of $\omega=2\pi\times 97$ Hz [20] corresponds to an oscillator width of $\beta\approx 2.13$ $\mu$m. The propagation velocity $v_z=v_0=\sqrt{2}$ osc. units (i.e., at the first mode threshold for transverse excitation, $E=1.5$ osc. units) equates to $v_z=1.84$ mm/s and a kinetic energy of 38.71 $\mu$K.

Figure 1 shows the spatial dependence of an equal superposition of two plane waves in the ground and first excited SHO modes ($a_0^2=a_1^2=1/2$). The total energy $E=1.51$ was chosen to be slightly above the first excited threshold. The phase fronts (i.e., lines of constant phase [21]) disappear at each hole in the wave function (i.e., where the probability density drops to zero), giving rise to a vortex and a $2\pi$ phase change in a closed loop around each hole. A surprising consequence is that a small amount of flux travels backwards along the waveguide even though both of the plane waves are travelling forward.

The longitudinal spacing of the oscillations depends on the total energy $E$. In the appendix of Ref. [17], we derived expressions for the spatial oscillations of expectation values for superpositions of plane waves such as those seen in Fig. 1. It was shown, in particular, that transverse oscillations of the probability density have a spatial period in the propagation direction $\gamma_z=2\pi/D_{v_z}$ due to the interference of the different velocity components $D_{v_z}=v_0-v_1$. In the present example $D_{v_z}=\sqrt{2.02}-\sqrt{0.02}$, giving $\gamma_z=4.91$. Increasing the total energy decreases $D_{v_z}$, thus increasing $\gamma_z$. This relation is utilized throughout this paper.

The dependence on the relative mode population is shown in Fig. 2 as the flux in the $z$ direction at $z=0$ with fixed $E=1.51$. The flux is shown since the velocity is undefined at the wave function holes. A two-mode wave function given by Eq. (3) with real, but nonzero coefficients $a_0$ and $a_1$ such that $a_1^2=1-a_0^2$, has holes located at

$$(x_h,z_h) = \left(-\frac{a_0}{\sqrt{2}a_1}, \frac{n\pi}{D_{v_z}}\right) \quad \text{for} \quad |n| = 0,2,\ldots,$$

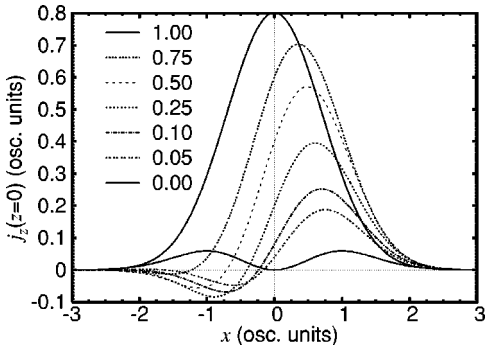


FIG. 2. The local flux in the $z$ direction of a superposition of two plane waves with equal total energy. The flux is plotted for $z=0$ to demonstrate the dependence of the flux on $a_0^2$ (the values are indicated in the figure). The values range from a pure $n=0$ mode ($a_0^2=1$, $a_1^2=0$) to a pure $n=1$ mode ($a_0^2=0$, $a_1^2=1$).

$$(x_h, z_h) = \left( \frac{a_0}{\sqrt{2}a_1}, \frac{n\pi}{D_{v_z}} \right) \quad \text{for} \quad |n| = 1,3, \ldots . \tag{4}$$

Note that the only effect of allowing $a_0$ and $a_1$ to be complex is a shift of $\delta/D_{v_z}$ in the positions $z_h$ of the holes by the relative phase $\delta$ between $a_0$ and $a_1$. There are also outer stagnation points at which both the flux and velocity are zero, but the probability density is nonzero. For $z=0$ this point occurs at $x_s=-(a_0 v_0)/\sqrt{2}a_1 v_1$, which is outside of the $z$ range shown in both Figs. 1 and 2. It does mean, however, that $j_z(x,z=0)$ is only negative in a region bounded by $x_s<x<x_h$. The dependence of the outer stagnation point on $v_0/v_1$ means that the spatial area where backflow occurs is dependent on both the total energy and the relative mode population.

The transition of $a_0$ in Fig. 2 between 1 and 0 mimics the vortex behavior in a wave packet. As a precursor to the wave-packet calculations shown in the next section, consider the following. A propagating wave packet (with a small energy spread) in a superposition of $n=0$ and $n=1$ modes with the same average total energy finds the $n=1$ component traveling slower than the $n=0$, which will eventually result in a pure $n=1$ component trailing behind the pure $n=0$ component. If the relative population of the two modes changes, so does the location of the vortices. As the two wave-packet components separate—corresponding to $a_0$ decreasing from 1 to 0 in the language used above—the vortices start out at $x_h=\pm\infty$ and end at $x_h=0$ [see Eq. (4)]. In the limit of small but nonzero $a_0$, the vortices form a line close to the center of the waveguide called a "vortex street" [2,18] and have alternating flux rotation. Throughout the separation of the wave-packet components, the longitudinal location of these vortices remains constant at $z_h=\pm n\pi/D_{v_z}$ since the total energy is fixed.

There is a useful experimental spinoff of the present plane-wave analysis for high-energy wave packets consisting predominantly of $n=0$ and $n=1$ modes. At high energies, $E \gg E_1$, a time-of-flight spatial snapshot of the wave packet would show the two modes propagating with approximately the same velocity $v_z \approx \sqrt{2E}$. In this case, the transverse oscillation occurs over a length scale $\gamma_z$ much larger than the oscillator width. In fact, such transverse oscillations have already been observed in a BEC after propagation through a waveguide perturbation [20]. Measuring $\gamma_z$ (which is independent of the relative mode population) would give not only $D_{v_z}$, but when combined with the time-of-flight velocity (which at high energies is independent of the mode) would also give the transverse trapping potential frequency $\omega$.

It may also be useful to note that while the flux profiles shown in Fig. 2 are dependent on the energy, the location of the probability density maxima in the $z=0$ cross section are only dependent on the relative mode population. Measurements of the transverse probability density profile such as the peak-to-peak amplitude shown in Ref. [20] can, at least in the low-density limit, give the relative population of the $n=0$ and $n=1$ modes along one transverse direction (given that the snapshot is a projection of the 3D density down to 2D). Note that a measurement of the transverse hole position [$x_h$ of Eq. (4)] is also independent of energy and can give the relative mode population. It may be difficult to resolve the exact hole location, however, so the peak-to-peak amplitude may be preferred for determining the population.

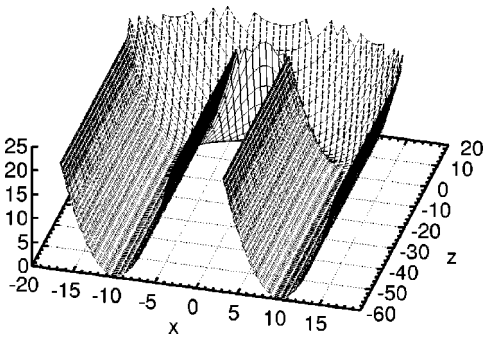


FIG. 3. Potential energy surface of a tight ($\rho_0=10$), 180° circular bend. Both the energy and coordinates are given in oscillator units. The coordinates are converted to the coordinate system of the incoming lead located at $x>0$, $z<0$, and this convention is used in the remainder of the paper.

## III. DETAILS OF THE CIRCULAR BEND CALCULATIONS

There are a number of atom chip wire configurations that can create curved waveguides [7,22], but we follow the ansatz adopted in Refs. [16,17]. That is, we assume a multiple wire configuration that does not require external bias fields applied in the plane of the microchip surface [23], so that the curved waveguide reduces to an effective 2D problem (assuming densities such that atom–atom interactions can be neglected).

We consider an idealized trapping potential for a circular bend of radius $\rho_0$ and angle $\phi_0$. The guiding potential is quadratic near the minimum, so SHO potentials are used here,

$$V = \begin{cases} \frac{1}{2}m\omega^2(x-\rho_0)^2, & z \leqslant 0, \\ \frac{1}{2}m\omega^2(\rho-\rho_0)^2, & 0 \leqslant \phi \leqslant \phi_0, \\ \frac{1}{2}m\omega^2(x-\rho_0)^2, & z \geqslant 0. \end{cases} \tag{5}$$

The two straight leads are described by Cartesian coordinates; and the circular bend, by polar coordinates. The potential for a tight ($\rho_0=10$), $\phi_0=180°$ bend, which is used throughout the remainder of this paper, is shown in Fig. 3. Such a tight, large angle bend emphasizes the effects of the bend.

Calculations using two different methods are used to examine vortices in the bends. First, since the 2D guiding potential of Eq. (5) is separable in each region, so is the Schrödinger equation, and time-independent interface matching calculations can be utilized. In this approach, wave transmission, reflection, and mode mixing are all a result of matching multimode plane waves at the boundaries between regions. This method has been described for waveguides with 2D [24,25] and 3D circular bends [16], and no further discussion is given here.

Second, time-dependent wave-packet calculations were performed using a split-operator Crank-Nicolson method

with finite differences [17]. An implementation on a uniform Cartesian grid (equally spaced in both the $x$ and $z$ directions) was adopted here instead of the hybrid nonuniform Cartesian and polar grid approach used in [17]. The computational overhead in including grid points that have large $V(x,z)$ is not an impediment for the $\rho_0=10$, 180° bend considered here. As the specific details of the present method follow from those outlined in Ref. [17], the interested reader is directed there.

The initial wave packet is a Gaussian centered at $(x,z)=(x_0,z_0)$, with spatial widths $\Delta_x$ and $\Delta_z$ and initial velocity $\bar{v_z}$:

$$\Psi(x,z,t=0)=N_0\, e^{i\bar{v_z}z}\, e^{-(x-x_0)^2/2\Delta_x^2}\, e^{-(z-z_0)^2/2\Delta_z^2}. \quad (6)$$

For an initial wave function centered at the SHO minimum, $x_0=\rho_0$, to be in the ground state of the SHO potential requires $\Delta_x=1$. Cigar-shaped wave packets ($\Delta_z \gg \Delta_x$) are used in the time-dependent calculations, which correspond to the experimental initial state in which the transverse trapping frequencies are significantly larger than the longitudinal trapping. The initial wave function is normalized using a midpoint integration rule [17], such that $\Sigma_{i,j}\delta_x\delta_z|\Psi(x_i,z_j,t=0)|^2=1$, where $\delta_x$ and $\delta_z$ are the grid spacings in each direction. Other expectations values were also determined using this integration rule.

The emphasis of the bend calculations shown in the next section is on energies so that only the first couple of excited modes are energetically accessible, greatly reducing the demands on the spatial grid compared to the grids required for the high-velocity wave packets seen in [17]. The grid spacings $\delta_x=\delta_z$ and time-step $\delta_t$ were chosen here so that variations in $\langle T\rangle(t)+\langle V\rangle(t)$ remained at levels less than 1 part in $10^6$. The extent of the spatial grid was always chosen so that the edges are never reached by the wave packet over the propagation time of interest.

## IV. CIRCULAR BEND CALCULATIONS

This section uses the bend shown in Fig. 3, i.e., a tight 180° bend with the SHO potential centered at $\rho_0=10$. The tight circular bend is a useful geometry to use to create the mode excitations (and thus vortices) since we could examine the transmission probabilities and vortex behavior exactly with the time-independent calculations before embarking on wave-packet calculations.

The transmission probabilities $T_{n_f,n_i}$ of plane waves traversing the circular bend are shown in Fig. 4 to show the ground state transmission and mode conversion from the ground state to higher transverse modes. Generally, there is minimal reflection except for a complete reflection spike due to a Feshbach resonance just below the first mode threshold at $E=1.5$ [16].

Based on the results shown in Fig. 4, two sets of circular bend calculations are presented in this section. For the first set, vortices in multimoded waves are examined at the peaks of $T_{1,0}$, namely energies of $E=2.225$ and $E=3.57$. These values were chosen to create a significant population of the $n=1$ mode while minimizing the population of $n>1$ modes,

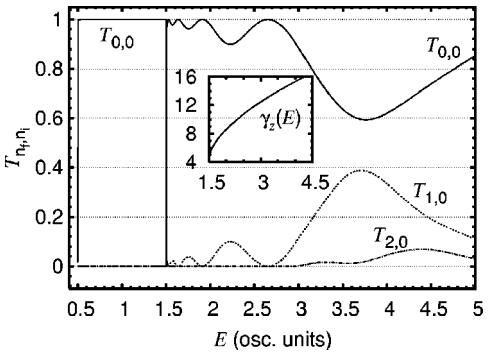


FIG. 4. Transmission probabilities $T_{n_f,n_i}$ of a $\rho_0=10$, $\phi_0=180°$ bend. The probabilities are shown for incoming waves in the ground state $n_i=0$ transmitted into the $n_f=0,1$, and 2 modes as a function of total energy $E$. The $n_f=3$ and $n_f=4$ modes are not shown since their $T_{n_f,n_i}\approx 0$ for these energies. Inset: spatial period $\gamma_z$ of superpositions of $n=0$ and $n=1$ plane waves as a function of total energy.

which makes the analysis simpler. Importantly, a tight bend means that significant mode excitation can occur at very low energies. Larger bends generally require larger propagation energies to obtain the same degree of excitation, but the interface matching method encounters convergence difficulties at higher energies due to the coupling to strongly closed modes [16,26]. In the time-dependent calculations, we use cigar shaped wave packets with average energies of 2.225 and 3.57 for comparison. Elongated Gaussian wave packet have a small velocity spread ($\Delta_z=10$ implies $\Delta v_z=0.1$), and the vortex dynamics are not obscured by wildly differing velocity components.

For the second set of calculations, waves with total energy $E\approx 1.5$ are used to explore the behavior of vortices in waves near the first excited mode threshold and the related Feshbach resonance. The tight 180° circular bend maximizes the width of the Feshbach resonance which is probed here using very energetically narrow wave packets ($\Delta_z=100$ implies $\Delta v_z=0.01$).

### A. Vortices in multimode wave propagation

The cleanest examples of interference vortices will be found when only the lowest two modes are populated. A tight circular bend approaches this ideal at $E=2.225$ where there are only two open modes and a significant excited mode probability and at $E=3.57$ where there are four open modes but only small $n=2$ and $n=3$ transmission probabilities. Specifically, the plane-wave calculations at $E=2.225$ give transmission probabilities of $T_{0,0}=0.899\,779$ and $T_{1,0}=0.100\,214$. At $E=3.57$, there is significant mode transfer from the ground to the first excited state: $T_{0,0}=0.615\,295$, $T_{1,0}=0.373\,943$, $T_{2,0}=0.010\,731$, and $T_{3,0}=2.7\times 10^{-5}$. At both energies the total reflection probabilities are less than $10^{-5}$.

The local phase and probability density contours of plane waves for these two energies are shown in Fig. 5, where the plane wave is incident in the top lead, and the transmitted waves exit in the bottom lead. For both energies, the vortices are located at the dents in the probability density contours. As was shown in Fig. 1, the phase fronts disappear at these

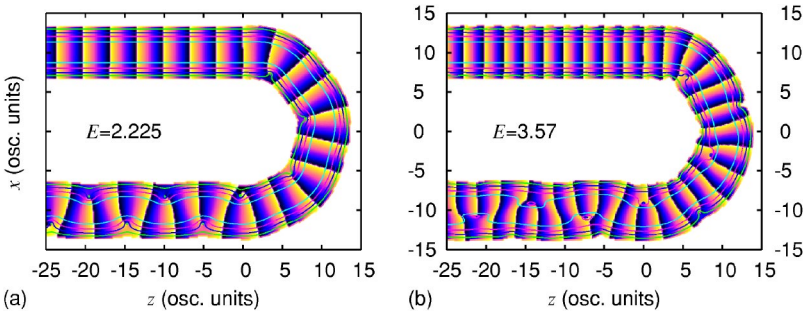


FIG. 5. (Color online) Local phase and probability density contours for plane waves incident in the top lead: (a) $E=2.225$ and (b) $E=3.57$. Vortices occur at the density contour indentations where the lines of constant phase disappear. Each density contour corresponds to an order of magnitude change in density. The phase convention is the same as in Fig. 1.

holes so that the total phase accumulated in a small closed loop about these holes is $2\pi$, i.e., a vortex.

There are two length scales in the propagation direction to consider. First, the distance between the phase fronts in the incoming lead is determined by the $n=0$ wavelength $\lambda_z = 2\pi/v_z$ where, for the two energies in Fig. 5, $\lambda_z=3.38$ and $\lambda_z=2.53$. Second, in the outgoing leads, the spatial oscillations in $z$ repeat every $\gamma_z=2\pi/D_{v_z}$ ($\gamma_z=9.6$ and $\gamma_z=14.2$). As the energy increases, $\lambda_z$ decreases while $\gamma_z$ increases. The inset of Fig. 4 shows the dependence of $\gamma_z$ across the energy range in question.

The holes in Fig. 5(a) are located further from the center of the waveguide than in Fig. 5(b) due to the differences in their excited mode populations, as predicted by the two-mode model in Eq. (4). The probability density also oscillates less regularly in the outgoing leads for Fig. 5(b) than for Fig. 5(a) due to the presence of about 1% of the $n=2$ mode (a two-mode calculation for $E=3.57$ shows more regularity). In both cases, vortices also appear within the bend due to a small amount of excitation to $n=1$ as the wave propagates across the entrance lead-bend interface. The eigenmodes within the bend are asymmetric with respect to the center of the SHO [16], and thus the vortices on the inside of the bend are located closer to the SHO center than the vortices on the outside of the bend. Crossing the exit lead interface creates additional mode excitation in the exit lead and more pronounced vortices.

Having observed vortices for plane waves, a natural question is whether they will be visible for a wave packet, or whether the velocity spread completely smears them out. Figure 6 shows the time-dependent behavior of cigar-shaped ($\Delta_z=10$) wave packets with average energies equal to those used in the time-independent calculations (initial average velocities $\bar{v}_z=1.857$ and $\bar{v}_z=2.4779$) propagating out of the same circular bend.

Each wave packet starts at $z=-100$ entirely in the ground state ($a_0=1$ and $a_1=0$ in the language used above). Per Eq. (4), the holes form at the sides of the wave packet as the excited mode becomes populated by the bend. In fact, to be visible in the plots we can estimate that $|a_1|^2$ must be at least $1/9$ for the holes to be within four oscillator units of the SHO center. The holes then migrate towards the center of the waveguide as the wave packet propagates and the local population in $n=1$ increases. Due to the difference in kinetic energy between the two modes, the $n=1$ mode increasingly lags behind, favoring $n=0$ at the leading edge and $n=1$ at the trailing edge, i.e., the ratio $a_0/a_1$ gradually changes across the length of the wave packet. As shown in Fig. 2 and predicted by Eq. (4), the transverse position of the vortices goes from $\infty$ to 0 as $a_0/a_1$ goes to 0, and we see this happen dynamically in a wave packet.

The parallel phase fronts in Fig. 6 show that the leading edge of the wave packet indeed consists of a nearly pure $n=0$ mode, seen as the parallel phase fronts in Figs. 6(a) and 6(h). That the trailing edge consists of nearly pure $n=1$ is most clearly seen as the $\pi$ alternating phase between each side of the SHO center in Fig. 6(d). For $\bar{E}=3.57$, the velocities of the $n=0$ and $n=1$ modes are closer than for $\bar{E}=2.225$, so the separation of the modes is not so dramatic as for $\bar{E}=2.225$ as each wave packet exits the bend. The snapshots in time for Figs. 6(e)–6(h) were chosen especially to highlight the transverse motion of the vortices from the edges towards the center of the waveguide as the wave packet propagates.

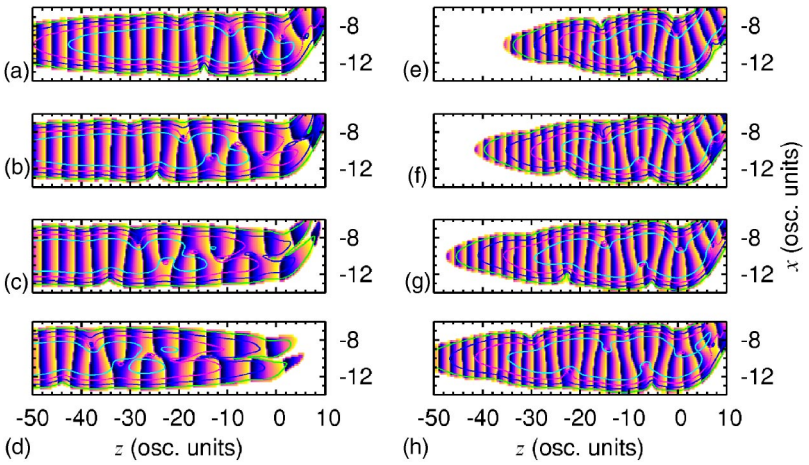


FIG. 6. (Color online) Local phase and probability density contours of wave packets exiting a $\rho_0=10$, $\phi_0=180°$ circular bend (the lead-bend interface is at $z=0$). Two calculations are shown at four snapshots roughly equally spaced in time: (a)–(d) show a $\bar{E}=2.225$ wave packet as time increases ($t=82.7$, 88.8, 94.9, and 101.05), while (e)–(h) show a $\bar{E}=3.57$ wave packet as time increases ($t=53.9$, 56.15, 58.4, and 60.65).

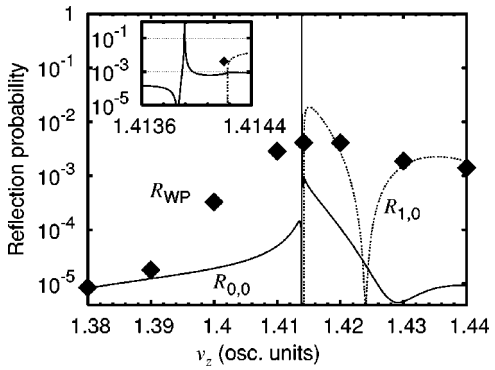


FIG. 7. Probability of a plane wave being reflected by a $\rho_0 = 10$, $\phi_0 = 180°$ circular bend as a function of incoming velocity (near the $n=1$ lead mode threshold at $v_z = \sqrt{2}$, i.e., $E=1.5$). The plane-wave reflection probabilities $R_{0,0}$ and $R_{1,0}$ are the solid and dotted lines, respectively. The diamonds are the total reflection probability $R_{WP} = R_{0,0} + R_{1,0}$ from wave-packet calculations. For the wave packets, the velocity denotes the average velocity $\overline{v_z}$ of the incident wave packet with fixed velocity spread $\Delta v_z = 0.01$. The inset highlights the resonance and threshold behavior.

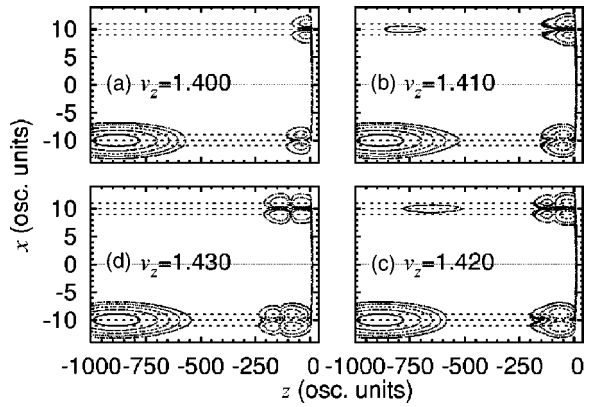


FIG. 8. Probability density of wave packets propagating with initial velocities $\overline{v_z} \approx \sqrt{2}$ near the $n=1$ threshold. The wave packets enter from the top lead with (a) $\overline{v_z} = 1.40$, (b) $\overline{v_z} = 1.41$, (c) $\overline{v_z} = 1.42$, and (d) $\overline{v_z} = 1.43$. The snapshots are taken at roughly the same average wave-packet position [i.e., at times of (a) $t = 1374.5$, (b) $t = 1364.5$, (c) $t = 1355$, (d) $t = 1345.5$]. Each line corresponds to an order of magnitude decrease in $|\Psi(x,y,t)|^2$. The position of the waveguide is indicated by the thin dotted lines.

It should be emphasized that although the wave packets are traveling forwards in the exit leads, there are small regions next to the holes that have backwards flowing flux (and not just relative to the wave-packet group velocity). For superpositions of $n=0$ and $n=1$ modes, these regions are towards the edge of the waveguide from the vortex. In a previous paper [17], we saw that under certain situations the Ehrenfest trajectory (i.e., the trajectory of a classical particle with initial conditions chosen to match the average position and average velocity of a wave packet) follows the probability density of multimoded wave packets as they traverse a circular bend. In the wave-packet snapshots seen in Fig. 3 of that paper, there are minima in the wave-function probability density as the wave packet exits a circular bend. Vortices were not discussed there since the wave-function dynamics are complicated by having significant population of $n>1$ modes—due to $\overline{E}=5$ (the transmission probabilities in Fig. 4). Multimoded oscillations were also seen in the split potential waveguide calculations of Jääskeläinen [27], but were not commented on in terms of the possible existence of vortices.

There are already experimental observations of transverse oscillations occurring after propagating BECs past an obstacle [20]. While taking probability density snapshots may show that wave-function holes have formed (which could be verified by examining the density along a transverse line), the real question may be whether velocity and/or phase sensitive imaging of propagating wave packets can be undertaken. This point was recently discussed in Ref. [28] for vortices in BECs, and there are a variety of well-established optics techniques that may enable the observation of interference vortices.

### B. Probing a Feshbach resonance

The circular bend modes have lower propagation thresholds than the lead modes, giving rise to a Feshbach resonance in the bend [3,16]. The resonance occurs at energies where the excited mode can propagate inside the bend but not in the leads. and causes 100% reflection when the energy of the incoming wave is exactly at the energy of the quasi-bound state. Plane-wave studies of vortices in hard-walled waveguides have shown that at such resonances there can be a dramatic reversal in direction of vortex rotation with only a small change in energy [3,10,18]. In the language of scattering theory, this reversal is just a consequence of the usual $\pi$ phase jump in the scattering phase shift at a resonance. We show local phase changes across the resonance for plane-waves incident on the bend, and compare these results to the dynamics of wave packets that energetically probe the Feshbach resonance.

#### *1. Reflection probabilities at resonance*

Previously, we demonstrated that a circular bend with SHO transverse confinement exhibits complete reflection due to a Feshbach resonance [16]. The specific results for a $\rho_0 = 10$, $\phi_0 = 180°$ bend are presented here to provide guidance. The first excited mode threshold in this bend occurs at $E = 1.498\,705\,9$, corresponding to a lead velocity of $v_z = 1.413\,298\,2$. The position of the Feshbach resonance peak is $v_z = 1.413\,903\,1$ and its width is only $0.000\,001\,7$ (in velocity). The reflection probabilities for plane waves in this velocity region are shown in Fig. 7.

The diamonds in Fig. 7 show the total reflection probabilities of elongated wave packets ($\Delta_z = 100$ and $\Delta v_z = 0.01$) with initial velocities near the first excited mode threshold at $v_z = \sqrt{2}$. Taking into account the velocity spread of the wave packet (which roughly translates into a convolution of the time-independent results), the time-independent and time-dependent results are consistent. Snapshots of the probability density after wave-packet propagation through the bend are shown in Fig. 8 for $\overline{v_z} = 1.40, 1.41, 1.42$, and 1.43. The initial location of all four wave packets was in the top lead at $z_0 =$

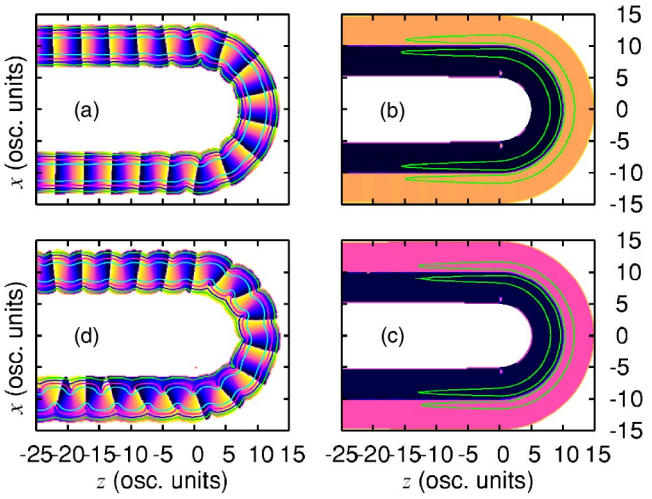


FIG. 9. (Color online) Local phase and probability density contours of four plane-wave solutions incident in the top lead with energies near the first excited mode thresholds. The velocities (a) $v_z=1.41$ and (d) $v_z=1.42$ are located on either side of both lead and bend $n=1$ thresholds, while (b) $v_z=1.413\,902\,4$ and (c) $v_z=1.413\,904\,0$ straddle either side of the reflection resonance. The resonant part of the wave function dominates in (b) and (c).

−1000. The local phase of the wave packet is not shown in Fig. 8 simply due to the huge disparity in the length scales of the wave packet compared to its wavelength ($\lambda \approx 4.4$).

As all four wave-packet velocities straddle both the lead and bend $n=1$ thresholds, a small amount of reflection is seen in both the $n=0$ and $n=1$ modes. The $n=1$ component of the wave function slowly exits the bend since it has a velocity barely above zero. There is a tiny amount of $n=0$ reflection, but it cannot unequivocally be attributed to the Feshbach resonance as the time-independent calculations show $R_{0,0} \approx 10^{-3}-10^{-4}$ on both sides of the mode threshold at $v_z=\sqrt{2}$. The fraction of velocity components in the wave packet in the resonance is also of the order $10^{-4}$. So, even though the Feshbach resonance results in 100% reflection, the width of the resonance is so small, it is almost impossible to observe a dip in the transmission to zero with a wave packet that has a finite energy spread. In the present example, the transmission shows less than a 1% dip in the transmission. To see a significant effect, a wave-packet velocity spread comparable to the resonance width is required, implying a wave packet on the order of $10^6$ oscillator units in length. Using the $^{23}$Na numbers from Sec. II, this would require an initial wave packet of width 2 $\mu$m and length 2 m, clearly an experimental challenge.

#### *2. Vortex reversal across resonance energies*

Although detailed measurements of the Feshbach resonance are unlikely, there remains the possibility of using vortices to simply detect whether a Feshbach resonance is present. For example, Fig. 9 shows the local phase of plane waves propagating with energies near the first mode threshold.

The $v_z=1.41$ and $v_z=1.42$ plane waves [Figs. 9(a) and 9(d), respectively], lie energetically on either side of both lead and bend $n=1$ thresholds, with the $v_z=1.42$ calculation displaying similar local phase characteristics to those seen in Fig. 5. For $v_z=1.41$ case, below both the lead and bend thresholds, mostly smooth, laminar flow through the waveguide is observed (since $T_{0,0}=0.999\,950$). The presence of evanescent modes in both calculations is seen as a perturbation of both the local phase and probability densities near the lead-bend interfaces. In fact, the presence of evanescent modes in Fig. 9(a) is enough to create vortices near the interfaces.

The two calculations with $v_z=1.413\,902\,4$ and $v_z=1.413\,904\,0$ [Figs. 9(b) and 9(c)] are just below and above the resonance and were chosen as the energies at which roughly 50% of the incoming flux is reflected. The single probability density contour shown is dominated by the $n=1$ transverse wave function associated with the Feshbach resonance. In the leads, the resonant wave function is evanescent and thus has a slow exponential decay, but the $n=0$ transmitted and reflected plane waves will eventually dominate far from the bend. Since the wave functions within the bend consist mostly of a slowly propagating $n=1$ mode with a very large wavelength, the phase evolves slowly around the bend.

Along the bend midpoint ($\phi=90°$, i.e., $x=0$) the local phase $\theta(x,z)$ abruptly changes from $1.361\pi$ to $0.361\pi$ in Fig. 9(b), and from $1.849\pi$ to $0.849\pi$ in Fig. 9(c). In both cases there is a rapid phase change of $\pi$ across the SHO minima, which appears consistent with a pure $n=1$ mode with a long wavelength. There is, however, a tiny fraction of the ground mode present, and a close examination of the flux direction (not shown here, but see the figures in Refs. [10,19]) reveals that there are a number of vortices along the $n=1$ valley. Each vortex is separated by a distance of $\gamma_z/2 \approx 2.2$, which comprises a vortex street within the bend that extends out into the leads due to the long exponential tail of the evanescent mode [18]. A tiny change in $v_z$ across the resonance results in a large change in local phase (between the two cases shown here approximately $\pi/2$) which corresponds to a reversal in the direction of the flux around the vortices.

The phase for $v_z=1.42$ is shown in Fig. 9(d). Previous studies of vortices in circular bends [10,18,19] implied that the Feshbach resonance was responsible for the creation of vortices, so it was initially surprising that vortices still appeared in the exit lead for a velocity so far from resonance. In fact, it was trying to understand why we observed interference vortices in the $v_z=1.42$ calculation that motivated much of the present paper.

The local phase for a $\overline{v_z}=1.41$ wave packet is shown in Fig. 10 for four snapshots in time. Figure 10(a) shows the wave packet entering from the top lead at $t=505$, while Fig. 10(b) shows the wave packet exiting at $t=804$ as a superposition of the $n=0$ and $n=1$ modes with a series of vortices forming near the exit lead interface. At $t=878.5$ [Fig. 10(c)] the $n=0$ component has largely left the bend, but a small residual amount remains, interfering with the $n=1$ component in/near the bend resulting in a vortex street. The final snapshot in Fig. 10(d) for $t=1719.5$ shows a small $n=1$ component slowly leaving the bend.

There are a number of processes that can manifest at large propagation times. For instance, the $n=1$ components slowly

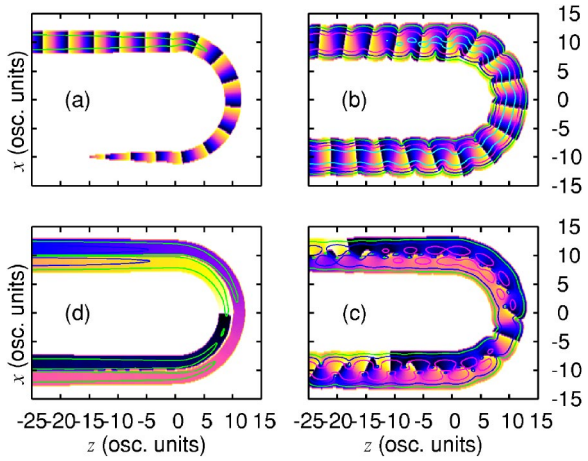


FIG. 10. (Color online) Local phase of a wave packet with initial velocity $v_z=1.41$ as it propagates through a tight circular bend. Four snapshots in time are shown: (a) $t=505$, (b) $t=804$, (c) $t=878.5$, and (d) $t=1719.5$. The probability density contours correspond to an order of magnitude decrease in $|\Psi(x,y,t)|^2$, with the cutoff chosen to be at $10^{-5}$ of the maximum density of the initial wave function. Note that the $v_z=1.41$ probability density at $t=1364.5$ was shown in Fig. 8.

leaving the bend cannot be from a Feshbach resonance (energetically forbidden). Any transmitted or reflected $n=1$ wave packet must instead simply be from part of the initial wave packet that had an energy above the $n=1$ threshold. The long-lived $n=1$ Feshbach resonance state will also slowly decay into $n=0$ plane waves and maintain vortices in and near the bend. At times between $t=878.5$ and $t=1719.5$ [Figs. 10(c) and 10(d)] the probability density and local phase slowly evolve while each vortex slowly moves into the waveguide center. Furthermore, we observe no change in the direction of flux rotation around a given vortex during the slow decay of remaining wavefunction out from the bend.

There is no definitive evidence that any of this phase and/or vortex behavior in the $\overline{v_z}=1.41$ wave packet is due solely to the Feshbach resonance. There remains the possibility that such effects are simply washed out by the velocity spread of the wave packet since the spread is large compared to the width of the Feshbach resonance. In contrast with the accuracy of the time-independent calculations (typically all energies converge to better than 1 part in $10^8$), however, it is unclear whether the present finite-difference calculations are even be able to represent such energetically narrow energy characteristics. For example, initial calculations of the very weakly bound states of circular bends using imaginary time propagation show a sensitive grid dependence with annoyingly slow convergence in energy, even in spatial grids far more dense those employed here.

## V. SUMMARY

Vortices have been shown to occur in multimoded waves of ultracold atoms propagating through waveguides in the limit of non-interacting atoms. Using a simple model with superpositions of forward propagating plane waves in straight waveguides, the vortices are seen to be a basic consequence of wave interference of the different modes. Given the wide variety of experimental atom chip waveguide configurations, our philosophy has again been to study a generic system using transverse SHO potentials. Using plane waves provides an analytic model that is simple to understand, and that revealed the dependence of the wave-function holes and backflow flux on the energy and mode population.

To generate multimoded waves using a realistic geometry, we employed a circular waveguide bend that enabled the energy dependence of the vortices to be examined using time-independent plane-wave calculations. Armed with this knowledge, we also performed wave-packet calculations to examine the time dependence of the vortices. A wave packet more closely reproduces the experimental conditions, as it is likely that most atom optical devices will not be supplied by atoms from a continuous source. Vortices were indeed seen in the wave packets, which are related to the sloshing of multimoded wave packets as they propagate along a waveguide. In a nutshell, the vortices form at the edges of the wave packet when mode excitation occurs, then smoothly migrate towards the center of the waveguide and form a string of vortices. If modes higher than $n=1$ are involved, then arrays of vortices can be formed, leading to multiple vortex streets.

The present results also provide some insight into current ultracold atom investigations, e.g., BEC propagation past a spatial defect in the waveguide [20], where transverse oscillations in the probability density have already been observed. Interference vortices should be present in the low-density limit and there is the possibility of directly detecting them using techniques to measure the local velocity field or the local phase across the wave packet. We have also suggested that the probability density snapshots of low-density ultracold atoms in a straight waveguide can provide information about the structure of the wave. The longitudinal oscillations give the relative velocity of the ground and excited modes which, when combined with a the absolute velocity from a time-of-flight measurement, gives the transverse binding frequency. The transverse position of the vortices gives information about the relative mode populations when only the ground and first excited modes have significant population.

The main problem with observing interference vortices with any method is that the regions of maximum backflow velocity are also the regions where the probability density is rather low. Experiments will probably observe the atom cloud a distance from the perturbation that creates the mode transfer, which will require high propagation velocities so that the modes do not separate. A high velocity increases the spatial length of the oscillations. Too high a velocity, however, and the outer stagnation point in the flux moves in towards the vortex, making it difficult to spatially resolve the backflow region. Another way to maximize the amount of backwards propagating flux would be to propagate the waves through perturbations such that only the ground and a significant percentage of the first excited modes are populated. While observing these interference vortices may prove to be rather like trying to see a green flash at sunset simply due to the small magnitude of the probability densities, these backwards propagating regions of a forward propagating multi-

moded wave packet nonetheless exist in the limit of noninteracting atoms.

On a fundamental tangent, while Feshbach resonances in circular waveguide bends are easily explored with plane waves, we were unable to find any definitive evidence of Feshbach resonant behavior in wave packets with realistic velocity spreads. The direct experimental observation of a resonant dip in the wave transmission that was observed using bent electromagnetic waveguides [29] would be virtually impossible to observe in the propagation of clouds of atoms through a microstructured waveguide bend. Our interest was driven by whether the dramatic local phase characteristics seen in plane-wave calculations across resonance energies would leave a measurable signature on a wave packet. We saw no such evidence in the present calculations. Feshbach resonances would be expected to occur in most microstructures where there is a potential well, and other geometries may produce a broader resonance that could be more easily explored than the circular waveguide bend.

The obvious extension of this research is examining the formation of hydrodynamic vortices [6] during propagation through microstructures, which could be generated via atom-atom interactions, and would presumably critically depend on the flow velocity.

## ACKNOWLEDGMENTS

This research was supported by the Department of the Navy, Office of Naval Research, and also by the Research Corporation. One of the authors (M.B.) would like to thank Professor Gary Wysin for a useful discussion on magnetic vortices, and Dr. Aaron Leanhardt for a critical reading of the manuscript.

[1] P. A. M. Dirac, Proc. R. Soc. London, Ser. A **133**, 60 (1931).
[2] E. H. Brandt, J. Vanacken, and V. V. Moshchalkov, Physica C **369**, 1 (2002).
[3] J. O. Hirschfelder and K. T. Tang, J. Chem. Phys. **64**, 760 (1976).
[4] E. J. Yarmchuk, M. J. V. Gordon, and R. E. Packard, Phys. Rev. Lett. **43**, 214 (1979).
[5] C. S. Lent, Appl. Phys. Lett. **57**, 1678 (1990).
[6] A. L. Fetter and A. A. Svidzinsky, J. Phys.: Condens. Matter **13**, R135 (2001).
[7] R. Folman, P. Krüger, J. Schmiedmayer, J. Denschlag, and C. Henkel, Adv. At., Mol., Opt. Phys. **48**, 263 (2002).
[8] J. Reichel, Appl. Phys. B: Lasers Opt. **75**, 469 (2002).
[9] H. Wu and D. W. L. Sprung, Phys. Lett. A **183**, 413 (1993).
[10] K. Berggren and Z. Ji, Phys. Rev. B **47**, 6390 (1993).
[11] J. O. Hirschfelder, A. C. Christoph, and W. E. Palke, J. Chem. Phys. **61**, 5435 (1976).
[12] J. O. Hirschfelder, C. J. Goebel, and L. W. Bruch, J. Chem. Phys. **61**, 5456 (1976).
[13] L. E. Helseth, Phys. Rev. A **69**, 015601 (2004).
[14] J. Ruostekoski, B. Kneer, W. P. Schleich, and G. Rempe, Phys. Rev. A **63**, 043613 (2001).
[15] T. Alexander and L. Bergé, Phys. Rev. E **65**, 026611 (2002).
[16] M. W. J. Bromley and B. D. Esry, Phys. Rev. A **68**, 043609 (2003).
[17] M. W. J. Bromley and B. D. Esry, Phys. Rev. A **69**, 053620 (2004).
[18] E. Simánek, Phys. Rev. B **59**, 10152 (1999).
[19] O. Olendski and L. Mikhailovska, Phys. Rev. E **67**, 056625 (2003).
[20] A. E. Leanhardt, A. P. Chikkatur, D. Kielpinski, Y. Shin, T. L. Gustavson, W. Ketterle, and D. E. Pritchard, Phys. Rev. Lett. **89**, 040401 (2002).
[21] J. F. Nye and M. V. Berry, Proc. R. Soc. London, Ser. A **336**, 165 (1974).
[22] J. H. Thywissen, M. Olshanii, G. Zabow, M. Drndić, K. S. Johnson, R. M. Westervelt, and M. Prentiss, Eur. Phys. J. D **7**, 361 (1999).
[23] X. Luo, P. Krüger, K. Brugger, S. Wildermuth, H. Gimpel, M. W. Klein, S. Groth, R. Folman, I. Bar-Joseph, and J. Schmiedmayer, e-print quant-ph/0311174 (2003).
[24] R. L. Schult, D. G. Ravenhall, and H. W. Wyld, Phys. Rev. B **39**, 5476 (1989).
[25] F. Sols and M. Macucci, Phys. Rev. B **41**, 11887 (1990).
[26] K. Lin and R. L. Jaffe, Phys. Rev. B **54**, 5750 (1996).
[27] M. Jääskeläinen, Ph.D. thesis, Royal Institute of Technology, Stockholm, 2003.
[28] M. Artoni and I. Carusotto, Phys. Rev. A **67**, 011602(R) (2003).
[29] J. P. Carini, J. T. Londergan, K. Mullen, and D. P. Murdock, Phys. Rev. B **46**, 15538 (1992).